alexpacini.com

Load- and Position-Independent Moving MHz WPT System Based on GaN-Distributed Current Sources

Alex Pacini, Alessandra Costanzo, Samer Aldhaher, and Paul D. Mitcheson

Author Accepted Manuscript

To cite this version:

A. Pacini, A. Costanzo, S. Aldhaher, and P. D. Mitcheson, "Load- and Position-Independent Moving MHz WPT System Based on GaN-Distributed Current Sources," *IEEE Transactions on Microwave Theory and Techniques*, vol. 65, no. 12, pp. 5367–5376, Dec. 2017, doi: 10.1109/tmtt.2017.2768031.

```
@article{Pacini_2017_TMTT_LoadandPositionIndependent,
  author  = {Alex Pacini and Alessandra Costanzo and Samer Aldhaher and Paul D. Mitcheson},
  title   = {Load- and Position-Independent Moving {MHz} {WPT} System Based on
             {GaN}-Distributed Current Sources},
  journal = {{IEEE} Transactions on Microwave Theory and Techniques},
  year    = {2017},
  volume  = {65},
  number  = {12},
  pages   = {5367--5376},
  month   = dec,
  doi     = {10.1109/tmtt.2017.2768031}
}
```

© 2017 IEEE. Personal use of this material is permitted. Permission from IEEE must be obtained for all other uses, in any current or future media, including reprinting/republishing this material for advertising or promotional purposes, creating new collective works, for resale or redistribution to servers or lists, or reuse of any copyrighted component of this work in other works.

Load- and Position- Independent Moving MHz WPT System Based on GaN Distributed Current Sources

Alex Pacini, *Graduate Student Member*, *IEEE*, Alessandra Costanzo, *Senior Member*, *IEEE*, Samer Aldhaher, *Member*, *IEEE*, Paul D. Mitcheson, *Senior Member*, *IEEE*.

***Abstract*—This paper describes the modeling, analysis and design of a complete (dc-to-dc) inductive wireless power transfer (WPT) system for industrial moving applications. The system operates at 6.78 MHz and delivers up to 150 W to a load moving along a linear path, providing a quasi-constant dc output voltage and maintaining a Zero Voltage Switching (ZVS) operation, regardless of position and load, without any retuning or feedback. The inductive link consists of an array of stationary transmitting coils and a moving receiving coil whose length is optimized to achieve a constant coupling coefficient along the path. Each Tx coil is individually driven by a constant amplitude and phase sinusoidal current that is generated from a GaN based coupled load-independent Class EF inverter. Two adjacent transmitters are activated at a given time depending on the receiver's position, this effectively creates a *virtual* series connection between the two transmitting coils. The Rx coil is connected to a passive Class E rectifier that is designed to maintain a constant dc output voltage independent of its load and position. Extensive experimental results are presented to show the performance over different loading conditions and positions. A peak dc-to-dc efficiency of 80% is achieved at 100 W of dc output power and a dc output voltage variation of less than 5% is measured over a load range from 30 Ohm to 500 Ohm. The work in this paper is foreseen as a design solution for a high efficiency, maintenance free and reliable WPT system for powering sliders and mass movers in industrial automation plants.**

***Index Terms*—Wireless power transmission, Inductive power transmission, Intelligent vehicles, Autonomous vehicles, Wide band gap semiconductors.**

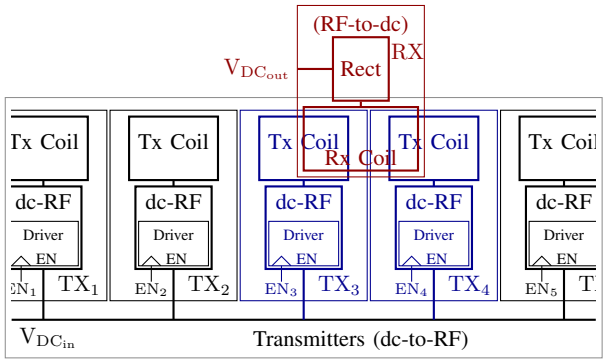
I. Introduction

INDUSTRIAL automation plants rely on machinery and tools for a wide range of processes and applications. Delivering power using cables to moving machines and tools can constrain their freedom of operation. In addition, a common failure mechanism in many applications is due to cable degradation and loose connectors, which occurs due to wear and tear from the repeated mechanical stress and pressure. Inductive WPT can enhance reliability and functionality [1]–[7], since the need of cables and connectors is reduced. WPT can also enable real-time machine testing, by combing wireless data and power transfer [8].

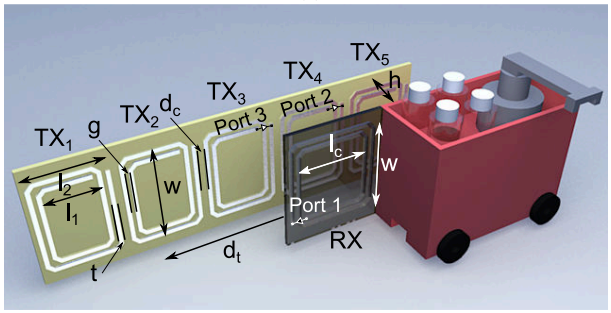
Manuscript received MM, 2017; revised MM, 2017; accepted MM, 2017.

A. Pacini and A. Costanzo are with the Department of Electrical, Electronic and Information Engineering "G. Marconi" (DEI) of the University of Bologna, Italy. A.Costanzo is also with ARCES (e-mail: alessandra.costanzo@unibo.it). S. Aldhaher and P. D. Mitcheson are with the Control and Power Group of the Imperial College, London (UK) (e-mail: paul.mitcheson@imperial.ac.uk)

This paper is an expanded version from the 2017 International Microwave Conference, Honolulu, HI, 4–9 June 2017.



(a)



(b)

Fig. 1. Moving WPT link powered by a linear array of planar Tx modules: a segment of five is shown, but the system can be extended to cover any linear path. Only two Tx are active at each time (blue), depending on the Rx (red) position. (a), block diagram, (b), rendered illustration of an industrial slider. For the present design at 6.78 MHz, the dimensions in cm are: $l_c = 17.2$, $l_1 = 12$, $l_2 = 18$, $d_c = 2$, $w = 24$, $g = 1$, $t = 1$ and $h = 6$.

A key feature of a dynamic WPT system is the ability to deliver consistent performance over different loads and positions, while maintaining high efficiency and constant output voltage. Current solutions in the literature show excellent efficiencies but only for static scenarios and at fixed loads as they are strongly dependent on the receiver's position. In [9] a wide range of operating frequencies for resonance tracking is required. To overcome the problem of variable couplings, a long single transmitting coil is adopted in [10], but it suffers from low efficiency due to the huge leakage inductance, which decreases its kQ product [11]. A segmented system composed of multiple active Tx coils is proposed in [12], [13], but the powering and receiving sub-systems are not detailed. [14] proposes six Tx coils always powered and connected in parallel. However, parallel-connected Tx coils have been demonstrated to be a sub-optimal solution, if the Tx-to-Rx distance is variable [15], [16]. Multiple active transmitters are also proposed in

[17], but again this approach is still limited to the description of the RF link alone. Furthermore a long feeding line is needed for powering, hence increasing the parasitic inductances. A way to solve misalignment issues in a limited path is introduced in [18], but a parallel connection of the Tx coils is still adopted.

This work expands upon [19], where the model of a novel modular moving WPT system is proposed. It consists of distributed RF power sources driving an array of stationary transmitting Tx coils, with one pair of Tx coils virtually series-connected and active at a time, depending on the sliding Rx module position. This contribution provides the entire dc-to-dc system design and characterization together with its experimental evaluation. New design solutions are adopted to comply with the actual behavior of each sub-system block. The full experimental characterization of the Class EF inverter in coupled configuration is discussed and the experimental results are provided. Important aspects of the actual implementation of the system are highlighted, that were not evident from the theoretical and numerical analysis presented in [19]. The critical impact of the coupled inverters output current phase imbalance is discussed in detail and confirmed by measurements. On the mobile receiver side, the rectifier is re-designed as a Class E topology instead of a Class EF, which also maintains zero reactance and constant voltage, as required by the coupled inverters but with a higher efficiency and a larger C_1.

The design starts by optimizing the inductive link to achieve a position independent coupling coefficient. This is done by selecting the optimum Rx coil geometry with respect to the Tx coil as shown in [15]. A pair of Tx coils are series connected, *virtually*, by means of identical coupled load-independent Class EF inverters. GaN HEMT are used to achieve improved efficiencies and higher power densities, with the system switching at $6.78\,\mathrm{MHz}$. A Class E rectifier is then designed by means of the nonlinear Harmonic Balance technique to ensure a quasi-resistive input impedance and a constant dc output voltage for all the Rx positions and dc loads of interest. In this way, a fully modular and periodic WPT system, whose length can be arbitrarily extended depending on the specific need, is demonstrated to be possible. A further added value of the proposed architecture is that only a dc feeding line and the control logic signals are needed along the powering path. In this way, any undesired reactive parasitic effects and RF losses along the path are absent and high WPT operating frequencies are enabled. A representative slice of the modular moving WPT system, consisting of four complete Tx modules and one Rx receiver sliding over them, is prototyped and an extensive experimental characterization is presented to validate the design procedure.

For the demonstrative part of the system design the activation/deactivation of the switches is performed manually. These operations can be straightforwardly implemented by a suitable control logic unit driven by the sensing of the Rx position. The inverters are easily synchronized by driving them with the same gate signal. Since the switching mechanisms are already fully accounted for, the system efficiency is not expected to be influenced.

Given the high operating frequency of $6.78\,\mathrm{MHz}$, the moving WPT system is tested in a quasi-static regime approximation, that is by means of snapshots of the receiver positions. Indeed, the switching period is orders of magnitude shorter than the Rx time-of-flight between two Txs.

II. Co-design of the entire moving WPT link

This section describes the theoretical and numerical approaches for the piece-wise design of a modular moving inductive WPT system. The goal is to achieve a position-independent coupling coefficient resulting in a constant DC output voltage regardless of load and position. Fig. 1(a) shows a block diagram of the system which consists of three main blocks (or subsystems): i) the still inverters (dc-to-RF); ii) the inductive WPT link (RF-to-RF); iii) the moving rectifier (RF-to-dc).

A. Electromagnetic Design of the RF-to-RF link

To solve the issue of variable couplings in a dynamic WPT system, an array of coils is used at the Tx side, [15], [16]. This choice allows a more efficient powering of the sliding path compared to long single transmitting coil. By connecting in series two transmitting coils at a time and by optimizing the Rx coil layout, a position-independent coupling coefficient is obtained. In [15] it has been analytically and experimentally demonstrated that the flat coupling coefficient behavior is retained also for various Rx vertical distances.

The system illustration of Fig. 1(b) shows the fixed array of planar Tx coils, at a prescribed distance from each other, facing the moving Rx. The geometrical dimensions, optimized for $6.78\,\mathrm{MHz}$, are reported in the figure caption. They are obtained by optimizing a set of three-port networks composed of two active Tx coils and a moving Rx one for constant coupling coefficient. Each three-port represents the system with a different l_c and a different Rx position. Twenty different receiver positions and the associated three-port networks are considered, with the receiver axis moving from $20\,\mathrm{cm}$ to $30\,\mathrm{cm}$ (see Fig. 2). The space-periodic path is schematically represented in Fig. 2, where the active coils are outlined depending on the Rx positions. In case (I) only TX_2 and TX_3 are powered. The Rx movement from $30\,\mathrm{cm}$ to $40\,\mathrm{cm}$ can be derived by mirroring the previous one, due to the symmetry.

When the receiver axis aligns with the TX_3 axis, case (II), TX_2 must be turned off and TX_4 must be activated, allowing to periodically reproduce the same behavior from $20\,\mathrm{cm}$ to $40\,\mathrm{cm}$. Therefore, the spatial periodicity of the system enables a theoretically unlimited path. By connecting in series the two active Tx coils, see Fig. 3, the interaction between the magnetic fields allows the resulting shared flux at the receiver coil to be constant.

The initial Rx coil length, l_c^{opt}, is computed geometrically in ideal conditions by means of the following relationship:

$$l_c^{opt} = l_1 + \frac{l_2 - l_1}{2} + d_c. \tag{1}$$

which is valid if the coils are assumed to be solenoids having the same current, hence a uniform magnetic field inside them and zero outside. Ideal conductors are assumed and all the parasitic effects are neglected. By segmenting the coil turns

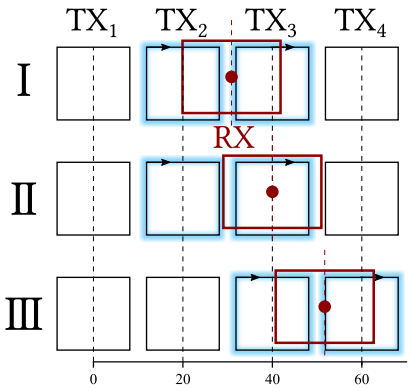


Fig. 2. A pair of series-connected Tx coils, in blue, with respect to the Rx positions (cm), in red. I and III correspond to all the Rx coil positions located between two subsequent Tx coils. II shows the Rx position where Tx coils switching is needed: TX_2 is deactivated and TX_4 activated. The sequence is repeated all over the transmitting path.

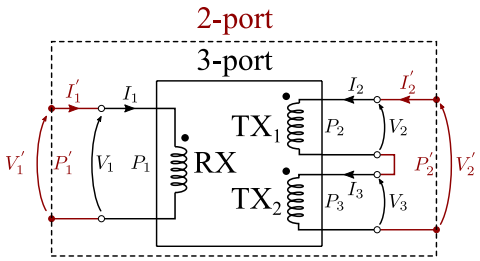


Fig. 3. Equivalent circuit of the instantaneous RF link: the 3-port network, representing two independent active Tx coils coupled with the Rx one, reduces to a 2-port network when the Tx coils are series-connected.

into elementary areas, the overall shared magnetic flux can be calculated by means of superposition of the elementary contributions. The optimum value of $l_c = l_c^{opt}$, is derived by assuming that when the receiver slides to the right, the flux lost at its left end side is exactly reintroduced at the right end side. Afterwards, realistic coils are used in a full wave EM simulation [20] of the RF link layout, to derive the $\boldsymbol{Z}$ matrix of the three-port network of Fig. 3. By recalling the generic coupling coefficient of two coils, L_a and L_b, with mutual inductance M_{ab} :

$$k_{ab} = \frac{M_{ab}}{\sqrt{L_a L_b}}. \tag{2}$$

The imaginary parts of $\boldsymbol{Z}$, $X_{ij} = \mathrm{Im}\{Z_{ij}\}$, are used to compute the three coupling coefficients characterizing the RF link (see Fig. 3), one between the two Txs, k_{TX}, and two between each Tx and the Rx, k_{RX_1} and k_{RX_2}:

$$k_{RX_1} = \frac{X_{12}}{\sqrt{X_{11}X_{22}}},\ k_{RX_2} = \frac{X_{13}}{\sqrt{X_{11}X_{22}}},\ k_{TX} = \frac{X_{23}}{X_{22}} \tag{3}$$

with $X_{22} = X_{33}$, since the transmitters are assumed identical. After the series connection of the two Tx coils ($I_2 = I_3 = I_2^{'}$, $V_2 + V_3 = V_2^{'}$, $I_1 = I_1^{'}$), the resulting *virtual* two-port network relationships are obtained:

$$\begin{aligned} V_1^{'} &= Z_{11} I_1^{'} + (Z_{12} + Z_{13})\, I_2^{'} \\ V_2^{'} &= (Z_{12} + Z_{13})\, I_1^{'} + (Z_{22} + Z_{23} + Z_{23} + Z_{22})\, I_2^{'} \end{aligned} \tag{4}$$

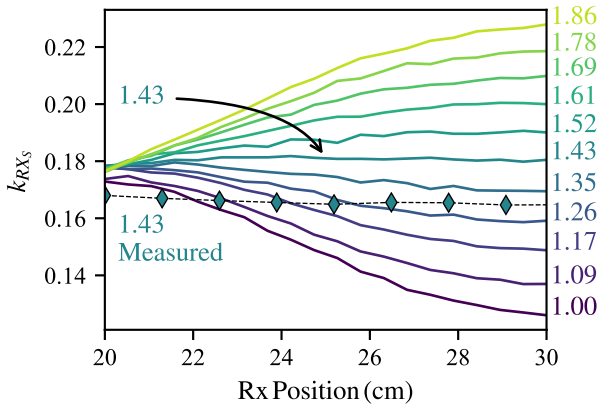


Fig. 4. Coupling coefficients of the *virtual* 2-port for different normalized Rx coil l_c/l_1 versus variable Rx displacements: 20 cm corresponds to the Rx axis aligned with the TX_2 axis and 30 cm to Rx axis located in the middle of the TX_2 and TX_3 axes. The displacement is given in cm to avoid confusion in the following, but can be normalized to l_1 as well. Only for $l_c/l_1 = 1.43$, k_{RX_S} does not varies all over the Rx path. The diamonds are the corresponding measured data. The Rx plane distance from the Tx plane is $h/l_1 = 0.5$ ($h = 6$ cm, see Fig. 1).

where reciprocity holds. Simplifying Eq. (4), the coupling coefficient of the RF link after the two Tx series connection is derived:

$$k_{RX_S} = \frac{1}{\sqrt{2}} \frac{k_{RX_1} + k_{RX_2}}{\sqrt{1 + k_{TX}}}. \tag{5}$$

The predicted impact of l_c on the link coupling coefficient, as the Rx is moving, is plotted in Fig. 4 with the normalized length l_c/l_1 as a parameter. Normalized plots allow an agile scaling of the whole system without affecting the performance as long as the parasitic effects are negligible. From Fig. 4 it is clear that $l_c/l_1 = 1.43$, which corresponds to $l_c = 17.2$ cm, ensures a constant coupling all over the sliding path, thus confirming the validity of the approximated approach introduced by (1). The corresponding measurements are superimposed in Figs. 4 and 5: an excellent flatness of k_{RX_S} is observed for the selected l_c. Details of the set-up are discussed in Section III. Finally, k_{RX_S} with l_c^{opt} is computed for different Rx-Tx distances h and the associated plots are shown in Fig. 5, confirming that l_c^{opt} ensures position independent performances. The measured data, for $h = 6$ and 10 cm, are superimposed in the same figure: slightly lower values of k_{RX_S} have been experimentally obtained, but the flatness is confirmed for any Rx height. $h = 6$ cm is selected for the prototype.

It should be noted that the demonstrated constant coupling coefficient is obtained by the concurrency of the layout optimization, that ensures the spatial periodicity, and the series connection of two transmitters, that are satisfied by a moving system along a linear path. On the contrary, a rotation or a lateral displacement that deviate the system from such periodicity can cause a degradation of the coupling coefficient.

B. Coupled Class-EF Inverters for Constant RF Current

To ensure the series connection of the active couple of Tx coils, while keeping the full modularity of the transmitting system, a coupled load-independent Class EF inverter, similar to the one proposed in [21] is adopted as the power source of each Tx coil. This topology is reported in Fig. 6, where two

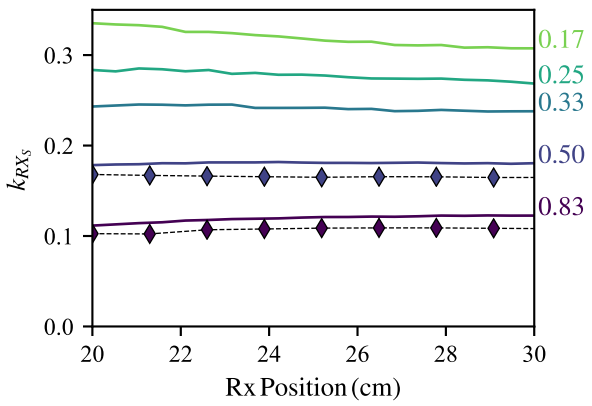


Fig. 5. Coupling coefficient of the *virtual* 2-port with $l_c/l_1 = 1.43$ for different distances h/l_1. The displacement is given in cm to avoid confusion in the following, but can be normalized to l_1 as well. The series connected link maintains its position-independent coupling coefficient at any Rx height (see Fig. 1). Diamonds are the measured data.

identical inverters driving two coupled inductors are shown: each inverter consists of a single GaN HEMT (Q_1), with a parallel reactive network designed to ensure ZVS operation. In a first step, the Rx is not yet considered, or, equivalently, $k_{RX_S} = 0$.

The ZVS is accomplished by the parallel connection of the output capacitance C_1 with the series branch $C_2 - L_2$, which is optimized to resonate at a frequency between the inverter switching frequency, 6.78 MHz, and its second harmonic. When S_1 is open, C_{3_1} and C_{3_2} are connected in series with the Tx coil L_3, to provide the proper residual inductance. This topology maintains the ZVS operation, while achieving a constant output current, for a wide range of loads without any need of re-tuning or components replacement. The useful feature of this inverter, to be exploited in the present distributed WPT system, is to provide a constant load-independent RF output current, enabling the *virtual* series connection of the two Tx coils.

First, following the numerical procedure presented in [21], the circuit parameters for the stand alone inverter are obtained: $L_1 = 88\mu H$ (RF Choke), $L_2 = 270nH$, $L_3 = 1.42\mu H$, $C_1 = 830pF$ (which includes the capacitance of Q_1), $C_2 = 718pF$, $C_3 = 480pF$, duty-cycle $D = 0.32$. In such conditions, the proper inverter resistive load can vary between 0 and 6 Ω.

When two nearby Tx coils are powered, the coupling between them, k_{TX} in Fig. 6, significantly modifies the load impedance of each inverter and the standalone topology can be used only as a starting point for the design of the two coupled inverters. Assuming the same L_3 for the two inverters, the coupled inverter design can start from the voltages and currents relationships at Tx coil ports:

$$\begin{aligned} V_{L_3(1)} &= (R_{L_3} + j\omega L_3) I_{o(1)} + j\omega M_{TX} I_{o(2)} \\ V_{L_3(2)} &= j\omega M_{TX} I_{o(1)} + (R_{L_3} + j\omega L_3) I_{o(2)}, \end{aligned} \tag{6}$$

where L_3 and R_{L_3} are the coils inductance and loss resistance, respectively, and $M_{TX} = k_{TX} L_3$. The currents $I_{o(2)}$ and $I_{o(1)}$, that ideally should be the same, if the assumption of *virtual* series connection holds, can be expressed as:

$$I_{o(1)} = A e^{-\frac{j\phi}{2}} I_o, \quad I_{o(2)} = B e^{\frac{j\phi}{2}} I_o, \tag{7}$$

where $A, B \in \mathbb{R}^+$, $\phi \in \mathbb{R}$ and $I_o \in \mathbb{C}$. Using (6), each Tx coil impedance, $Z_{L_3(n)}$ with $n \in \{1, 2\}$, in the absence of a receiver can be computed as:

$$Z_{L_3(n)} = \frac{V_{L_3(n)}}{I_{o(n)}} = R_{L_3} + j\omega L_3 + j\omega M_{TX} \alpha_n, \tag{8}$$

where $(\alpha_n) = (\alpha_1, \alpha_2) = \left(B/Ae^{j\phi}, A/Be^{-j\phi}\right)$.

The actual inductances at each inverter output, $L_{TX(n)}$, taking into account the coupling are:

$$L_{TX(n)} = \frac{\mathrm{Im}\left\{Z_{L_3(n)}\right\}}{\omega} = L_3 + |\alpha_n| M_{TX} \cos(\phi). \tag{9}$$

Thus, accounting for the Tx coils coupling is mandatory, because the effective inductances, loading each coupled inverter, are different from those at the output of a standalone inverter.

Furthermore, differences in the current phases (ϕ) of each coupled Tx coil result in power transferred between the inverters ($P_{t(n)}$) that can be evaluated using the real part of (8):

$$\mathrm{Re}\left\{Z_{L_3(n)}\right\} = R_{L_3} + \omega M_{TX} |\alpha_n| \sin(\phi_n), \tag{10}$$

$$P_{t(n)} = \omega M_{TX} |\alpha_n| \sin(\phi_n) \left|I_{o(n)}\right|^2, \tag{11}$$

where $(\phi_n) = (\arg\{\alpha_1\}, \arg\{\alpha_2\}) = (\phi, -\phi)$.

Since $P_{t(1)} = -P_{t(2)}$, the linear network alone does not introduce losses, but if the inverter is included, a phase difference can compromise its ZVS operation due to an additional voltage component induced from the current through the coupled coil that is not synchronized with the inverter operation. Indeed, the switching clocks of both inverters are synchronized (or supplied from a common source) by design and an unwanted induced voltage is inevitably affecting the ZVS. The closed switch shorts this induced voltage, causing high currents and losses. Moreover, a variation of the residual inductance, as in (9), even if negligible for small phase impairments, affects the ZVS due to detuning since the inverter is not tolerant to variations of its reactance termination. On the contrary, a current magnitude variation, $|\alpha_n|$, produces similar effects on the ZVS but only due to the residual inductance, because, without any phase impairment, the power transferred between the Tx coils is always zero ($\sin(\phi_n) = 0$). Besides an efficiency degradation, this also means that Q_1 can experience overheating.

The quality factor of the virtual inductor $L_{TX(n)}$ is:

$$Q_{L_{TX}(n)} = \frac{\omega \left(L_3 + |\alpha_n| M_{TX} \cos(\phi)\right)}{R_{L_3} + \omega M_{TX} |\alpha_n| \sin(\phi_n)}, \tag{12}$$

or equivalently, using the relation $M_{TX} = k_{TX} L_3$:

$$Q_{L_{TX}(n)} = \frac{1 + |\alpha_n| k_{TX} \cos(\phi)}{Q_{L_3}^{-1} + |\alpha_n| k_{TX} \sin(\phi_n)}, \tag{13}$$

where $Q_{L_3} = (\omega L_3)/R_{L_3}$ is the quality factor of L_3.

Since a key feature is to achieve currents with equal amplitudes, it is possible to approximate $|\alpha_n| \simeq 1$. Therefore:

$$L_{TX(n)} \simeq L_3 + M_{TX} \cos(\phi) \simeq L_3 + M_{TX}, \tag{14}$$

where $\cos(\phi) \simeq 1$ for small angles ϕ. Equivalently:

$$L_{TX(n)} \simeq L_3 \left(1 + k_{TX}\right). \tag{15}$$

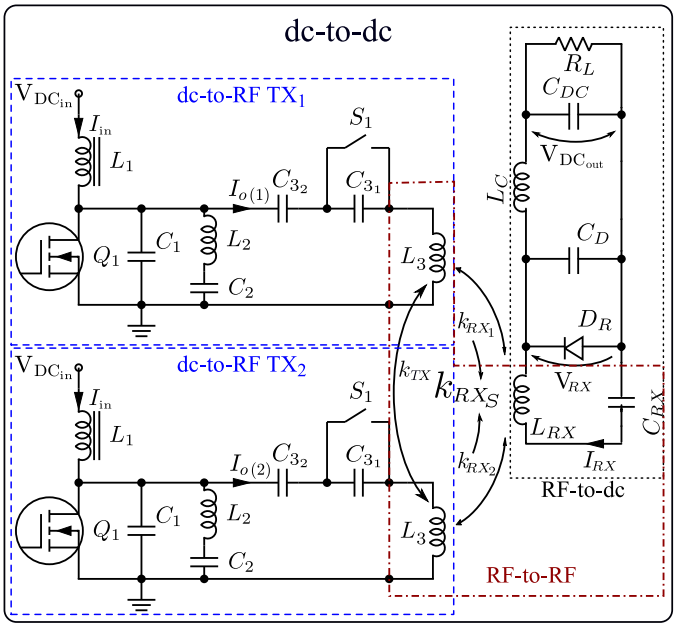


Fig. 6. *Instantaneous* dc-to-dc moving WPT system. On the Tx side, the dc-to-RF sub-system consists of two identical current sources exciting two coupled Tx coils, L_3. To form the RF-to-RF sub-system, they are coupled to the Rx coil, L_{RX}. On the Rx side, the RF-to-dc sub-system is a class E rectifier terminated on a resistive load (variable).

The resistive part becomes:

$$\mathrm{Re}\left\{Z_{L_{3(n)}}\right\} \simeq R_{L_3} + \omega M_{TX} \phi_n, \tag{16}$$

with $\sin(\phi_n) \simeq \phi_n$ for small angles ϕ_n.

For this setup, the Tx coils are modeled as: $k_{TX} = -0.0595$, L_3 =1.42 μH, R_{L_3} =0.15 Ω, $\omega = 2\pi 6.78 \times 10^6$rad/s. Since the coupling k_{TX} is negative, $L_{TX(n)}$ =1.34 μH, smaller than L_3.

The next step is to guarantee the proper residual inductance [22] to each coupled inverter. Let $L_{3,r}$ be the desired one for the standalone inverter, which is the result of the $C_3 - L_3$ series. When the *virtual* $L_{TX(n)}$ loads the inverter in place of L_3, the proper compensating capacitor $C'_{3(n)}$ which provides $L_{3,r}$ is computed as:

$$L_{3,r} = L_3 - \frac{1}{C_3 \omega^2}, \; L_{TX,r(n)} = L_{TX} - \frac{1}{C'_{3(n)} \omega^2}. \tag{17}$$

Forcing $L_{3,r} = L_{TX,r(n)}$ and using (15):

$$C'_{3(n)} = \frac{C_3}{1 + \left(\frac{\omega}{\omega_r}\right)^2 k_{TX}}, \text{ where } \omega_r = \frac{1}{\sqrt{C_3 L_3}}, \tag{18}$$

where C_3 is the optimal value for the standalone inverter [21] and $C'_{3(n)}$ is the corresponding one for the coupled case.

The last issue to be discussed is to limit the currents induced in the non-active Tx coils due to the currents flowing in the activated coils. From circuit simulation it is shown that without any countermeasure, these currents are of the same order of magnitude of the desired ones, resulting in additional losses and detuning of the active inverters. To minimize this contribution, the capacitor $C'_{3(n)}$ is split into two C_{3_2}, C_{3_1}, with $C_{3_2} > C_{3_1}$, and a switch (S_1 in Fig. 6) is connected in parallel to the smaller capacitor: if the inverter is off, the switch is closed, if the inverter is on, the switch is open. In this way, if the inverter is off, its load is strongly detuned and the resulting output current is minimized. Furthermore, this solution avoids to short the $V_{DC_{in}}$ supply, which would happen by shorting a single $C'_{3(n)}$. To determine C_{3_1} and C_{3_2} values, their series connection is chosen to be equal to $C'_{3(n)}$. Let $C_{3_2} = \beta C_{3_1}$, it follows that:

$$C_{3_1} = C'_{3(n)} \left(\frac{\beta + 1}{\beta}\right), \; C_{3_2} = C'_{3(n)} (\beta + 1). \tag{19}$$

A snubber, formed by R_S and L_S, is also connected in series to S_1 to mitigate the current peaks through the charged C_{3_1} when the switch is closed.

The designed values of these components are: C_{3_1} =530 pF, C_{3_2} =4.70 nF (hence $C'_{3(n)}$ = 480 pF and $\beta \sim 9$), R_S = 10 kΩ, L_S = 250 nH. An inactive Tx module is reported in Fig. 7.

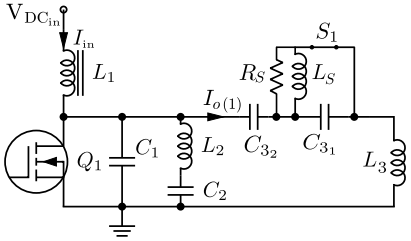


Fig. 7. Modified Class EF inverter in the off state: S_1 is closed, the inverter is detuned and the current $I_{o(1)}$ is negligible.

Fig. 6 shows the circuit schematic of the end-to-end (dc-to-dc) link with two active Tx modules and the Rx coil loaded by a Class E rectifier similar to the one designed and experimentally verified in [23], [24]. The modified design Class E rectifier is detailed in the next subsection.

In the next step, to evaluate the dc-to-RF sub-system in different positions, the receiver is introduced as a series resonant RLC load (with $k_{RX_S} \neq 0$), which allows to check if the coupled inverters sustain the same current through the Tx coils. It also allows to verify that the output voltage on the resistive load is independent from both the Rx position and the load. The values of the components at the Rx side are: L_{RX} =1.7 μH, C_{RX} =324 pF. k_{RX_1} and k_{RX_2} are derived by full-wave EM simulation of the coupled-coil 3-port RF link. From the measurements, the coupling coefficients resulted to be 10% lower than predicted, see Fig. 4, which in turn results in an effective k_{RX_S} of about 0.16.

First, the circuit of Fig. 6 is simulated in time-domain, with the rectifier replaced by a variable resistive load, for several receiver positions and loads: for each of the twenty Rx positions previously considered. The performance with respect to thirty different loads are evaluated, from 10 Ω to 1 kΩ. Fig. 8(a) shows the currents through each Tx coil, while Fig. 8(b) reports the voltage across the resistive Rx load. The input dc voltage ($V_{DC_{in}}$) is 70 V. All these plots are practically superimposed, proving that the coupled inverters are able to work as load-independent current sources, with the *virtual* series connection between the two Tx active coils confirmed.

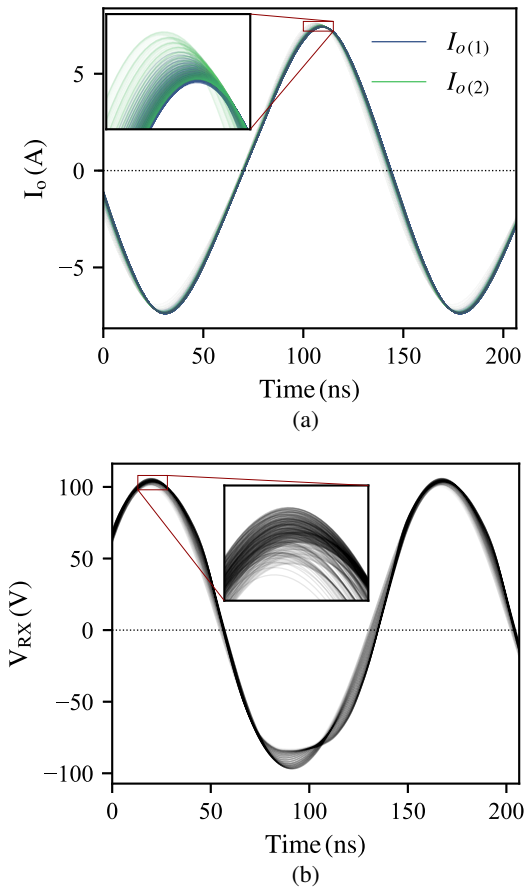


Fig. 8. Load and position independent waveforms of the currents exciting the two coupled Tx coils, Fig. (a), and voltages on the load (purely resistive and which replaces the rectifier in Section II-B), Fig. (b), for a $V_{DC_{in}}$ of 70 V. Results are from a set of 600 nonlinear/EM co-simulations spanning a 10 cm Rx displacement (20 different Rx positions) and 30 loads from 10 to 1 kΩ. The curves are almost indistinguishable, insets highlight the differences.

C. The Rectifier and the Complete dc-to-dc Link

To ensure the same performances discussed above, the rectifier is required to present a constant output voltage and a purely resistive input impedance, over the range of RF input power of interest, for any possible Rx position and loading conditions. This is a challenging task and, to the authors' knowledge, it is still unresolved. Indeed, the design of a standard Class E rectifier [22], [23] cannot be adopted for the present case, because its input reactance is dependent on the duty-cycle, which is a function of the dc load. Furthermore, in a moving system, such reactance varies with the Rx position and, once reflected to the Tx side, would degrade its performances, which are based on the (resistive-)load-independent coupled inverters. For a given excitation, the nonlinear reflected impedance $Z^{'}_{RX(n)}$, which effectively loads the inverter, can be written as:

$$Z^{'}_{RX(n)} = \frac{\omega^2 M^2_{RX(n)}}{Z_{RX}} \tag{20}$$

where $M_{RX(n)} = k_{RX(n)}\sqrt{L_3 L_{RX}}$ is the mutual inductance between an active Tx coil and the Rx one and Z_{RX} is the rectifier input impedance (V_{RX}/I_{RX}) at the fundamental harmonic. Since $M_{RX(n)}$ strongly depends on the Rx position, a constant imaginary part of Z_{RX} still produces a significant variation of $Z^{'}_{RX(n)}$ while the Rx is moving. Thus, the rectifier has to provide a quasi zero imaginary part of $Z^{'}_{RX(n)}$ for any dc-load of interest.

The Class-E Resonant Rectifier [25] with a quasi-resistive-input is used as a starting point. Although this solution is able to reduce the reactive part of Z_{RX}, by a proper choice of C_D and by allowing for a ripple of the output current by reducing L_C, it results in a output voltage strongly dependent on the dc load, which is not an acceptable solution for the system under consideration. For this reason an harmonic balance (HB)-based optimization of the whole dc-to-dc system is carried out, spanning all the possible Rx loads and positions. The RF choke, L_C, is reintroduced. The capacitors C_{RX} and C_D (Fig. 6) are included among the design variables. Two main goals are pursued: the maximization of the dc-to-dc efficiency and the minimization of the dc output voltage variations, which imply minimizing the imaginary part of $Z^{'}_{RX(n)}$. A total number of system configurations equal to 600 is considered, covering 20 Rx positions and 30 loads. The nonlinear regime is described using 16 harmonics. $V_{DC_{in}}$ is 70 V, which is the best trade-off between maximum output dc power, efficiency, and safety for the experimental verification. The losses are accounted for by resistances in series with the respective inductances and are computed as: R_{L_1} =2 Ω, R_{L_2} =0.06 Ω, R_{L_3} =0.15 Ω, $R_{L_{RX}}$ =0.2 Ω, R_{L_C} =2 Ω. Q_1 is modeled as a switch with a series resistance of 50 mΩ, while the remaining components are ideal. The other circuit elements are: L_{RX} =1.7 μH, L_C =88 μH, C_{DC} =20 μF. The diode is the Schottky SiC Wolfspeed/CREE C3D1P7060Q, chosen to sustain high current/voltage capability and has a low capacitance. To comply with high current peaks, two diodes are connected in parallel thanks to the positive temperature coefficient of SiC diodes, which results in equal sharing of currents, and are included in the simulation using their SPICE model. The optimized capacitors are: C_{RX} =498 pF and C_D =33 pF.

The predicted dc output power is 100 W on a 38 Ω load with a dc-dc efficiency of 80%, calculated as:

$$\eta = \frac{P_{DC_{out}}}{P_{DC_{in}}}. \tag{21}$$

The voltage variation is under 5%, for any load value over 30 Ω. After the nonlinear optimization, the imaginary part of the impedance $Z^{'}_{RX(n)}$, monitored for all the system configurations discussed above (Rx positions and loads) is always lower than $0.2j$, corresponding to a L_3 variation under 5 nH, or 0.3%. This ensures the proper switching operation (ZVS) of the inverters.

III. Experimental Set-Up and Measurements

The measurement set-up is composed of four identical Tx modules (one is shown in Fig. 10) and is reported in Fig. 9. Details of the inverter and the rectifier are shown in Fig. 11 and in Fig. 12, respectively. Q_1 is a GaN System GS66504B Enhancement HEMT GaN FET. The powering path, as extended as necessary, is obtained by placing side-by-side other transmitter modules, like "Lego" tiles. Therefore the system only requires a single dc-feed line along the whole path while the RF signal is generated on board at the active

modules locations only, which is a strong advantage in terms of power consumption.

On top of the transmitter path, the receiver unit is able to continuously slide through the Tx path. It is also possible to transfer power to multiple receivers using different pairs of inverters, by ensuring a pair of inactive coils in between two pairs of the active ones, to avoid unwanted multiple couplings.

In the prototyped Class E rectifier, the Wolfspeed/CREE C3D02060F diode is adopted in place of the two C3D1P7060Q, due to the inaccuracy of the SPICE model of the latter in describing the diode capacitance, which causes unwanted non-zero reactance at the rectifier input. This allows a lower capacitance, of the order of 20 pF, at the expense of a 1% reduction of the peak efficiency. However, this is found to be necessary to achieve a proper working system. Both devices are based on Wide Band Gap Semiconductors, which allow higher efficiencies, power densities, breakdown voltages, and low stray capacitances.

TABLE I
TX AND RX COMPONENT VALUES.

Inverter:	**Standalone [21]**	**Coupled**	
	Simulated	Simulated	Prototype
L_1	88 µH	88 µH	88 µH
L_2	270 nH	270 nH	283 nH
L_3	1.42 µH	1.42 µH	1.42 µH
C_1	830 pF	830 pF	660 pF
C_2	718 pF	718 pF	696 pF
C_3	480 pF	—	—
C_{3_1}	—	530 pF	526 pF
C_{3_2}	—	4.7 nF	4.7 nF
Q_1	50 mΩ (R_{on})	50 mΩ (R_{on})	GS66504B
R_S	—	10 kΩ	10 kΩ
L_S	—	250 nH	250 nH
k_{TX}	—	−0.0595	−0.0595
D	0.32	0.32	0.32
f	6.78 MHz	6.78 MHz	6.81 MHz
Rx load:	**Resistive**	**Rectifier**	
	Simulated	Simulated	Prototype
L_C	88 µH	88 µH	88 µH
L_{RX}	1.7 µH	1.7 µH	1.7 µH
C_D	—	33 pF	30 pF
C_{DC}	—	20 µF	20 µF
C_{RX}	324 pF	498 pF	498 pF
D_R	—	2 x C3D1P7060Q	C3D02060F

Table I reports all the component values of the inverters and of the receiver. Both the predicted and the actual ones used in the prototype are reported. For the Tx side, both the standalone and the coupled inverter configurations are reported. For the Rx side, two configurations are considered: i) the purely resistive variable load, in series with the $C_{RX} - L_{RX}$ resonator; ii) the rectifier. Some component values of the prototype are different from the predicted ones due to the fine tuning needed for the experimental setup. The optimum operating frequency of the prototype was found to be 6.81 MHz to achieve ZVS.

A. Entire WPT System Characterization with the Moving Rx

The receiver is moved over the entire Tx path and the dc output voltage is measured. Fig. 13(a) shows the simulated and

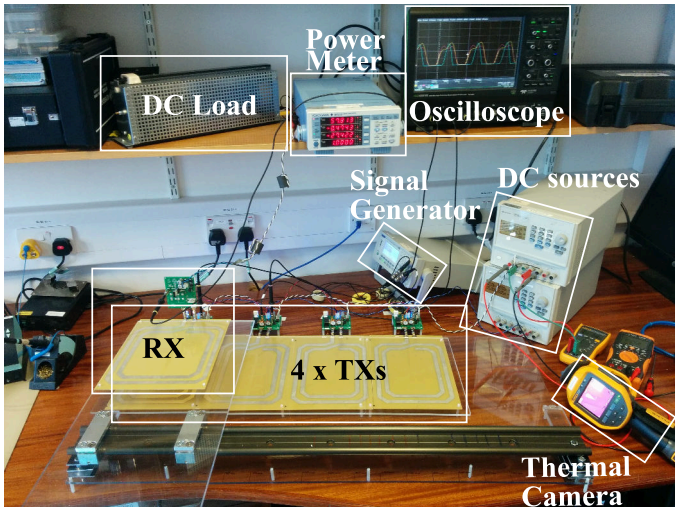


Fig. 9. dc-to-dc link set-up: four Tx coils, each one driven by its own inverter, with a Rx subsystem sliding over them at a vertical separation of 6 cm. The GaN FET is driven by an ISL5511IRZ high speed mosfet IC driver with a gate voltage of 5 V. The variable load is connected to the dc output and spans from 30 Ω to 120 Ω (higher resistances are obtained by a series connection of 100 Ω power resistors). The output dc power is measured by the Yokogawa WT310 power meter and the RF voltage waveforms are monitored using the LeCroy HDO4054 oscilloscope. The thermal camera is used for temperature monitoring.

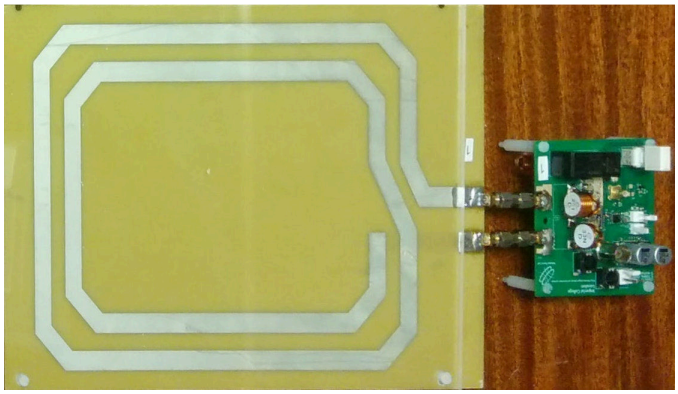


Fig. 10. Photo of a single TX module.

measured dc output voltage and Fig. 13(b) the overall dc-to-dc efficiency. Simulation results belong to two different models of the RF-to-RF link: the first one uses the link Z-matrix computed by full-wave EM simulation; the second one uses a coupled coils model with the coupling coefficient reduced by 10% ($k'_{RX(n)} = 0.9k_{RX(n)}$), which better matched the VNA measurements of the RF link, corresponding to a slightly longer Tx-Rx effective distance. The model with $k'_{RX(n)}$ is in very good agreement with the measurements. The key aspects of these experimental plots is the excellent flatness of $V_{DC_{out}}$ that the present design is able to ensure, regardless of the receiver position and load. Fig. 13(b) shows the efficiency compared again with the two simulation models. The maximum efficiency is 80% with an output power of 100 W. As previously stated, the goal of a 100 W is chosen for validating the design of the entire dc-to-dc system, while ensuring safe measurement conditions. A 70 V dc bias is needed to reach this output dc power. Choosing a higher dc bias increases the maximum efficiency and allows a higher output dc power and voltage,

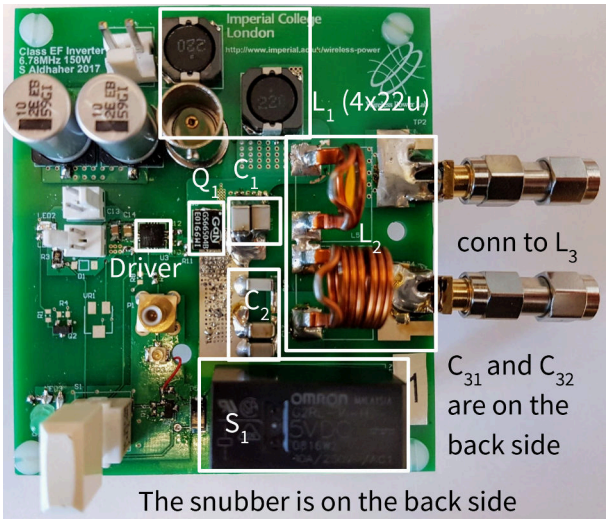


Fig. 11. Photo of the Class-EF inverter.

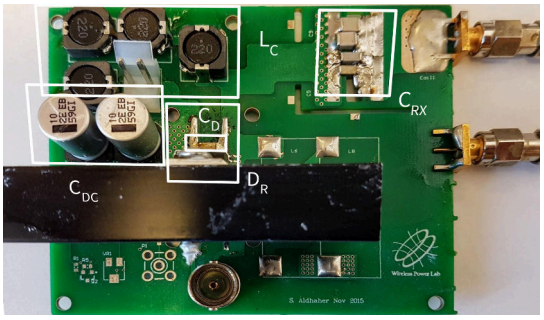


Fig. 12. Photo of the Class-E rectifier.

but with no added value to the design proposed in this work. The chosen GaN device allows the inverter to operate with voltages as high as 100 V, predicted by simulation to enable an output dc power of 160 W into a 35 Ω load, with a dc-to-dc efficiency of about 84%. The maximum dc voltage is actually not limited by the GaN and SiC devices, but by the overheating of L_2, which reaches 80 °C with a 70 V input.

Fig. 14 shows the measured dc output voltage versus an Rx path, which exceeds the design path and highlights that the flatness property is ensured only if the *virtual* series connection is guaranteed, while it is lost as soon as the the receiver moves out of the design path. Fig. 15 reports the measured voltage across D_R: the peak value of 300 V is well below the 600 V breakdown voltage and the duty-cycle is only slightly modified (less than 6%) by load changes, ensuring an almost constant dc component of the voltage across the diode, without any output current ripple.

A loss budget can finally be estimated by considering constant (for the system in idle mode) and variable (with the output power) losses. With regard to the first contribution, the measured idle power loss for both coupled inverters is 15 W. The simulated current flow in L_2, which is the components experiencing the highest temperature, is in the order of 10 A, resulting in a 3 W power loss. The power loss due to a simulated current of 7 A through L_3 is 3.5 W.

The losses variable with the output power are mainly affected by the RF chokes and are also position-dependent: when the Rx

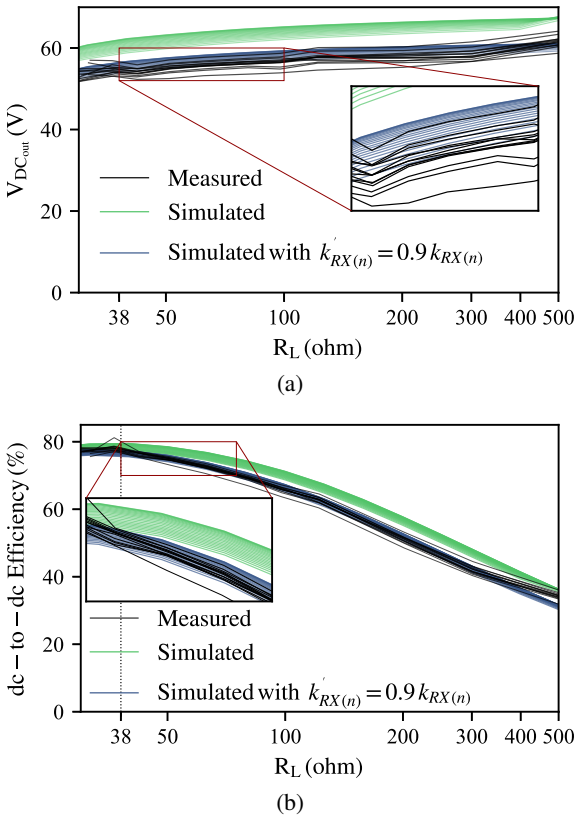


Fig. 13. (a) measured and simulated output dc voltage and (b) system efficiency versus dc load, for twenty positions over a 60 cm Rx displacement. For 0 cm, the Rx and TX_1 axes are aligned; for 60 cm, the Rx and TX_4 axes are aligned. The curves are almost indistinguishable (for a given load no significant variations of the system performance are experimentally verified). Insets are used to highlight the differences. The two families of simulated plots are obtained using $k_{RX(n)}$, as computed in (5), and with $k'_{RX(n)} = 0.9k_{RX(n)}$, which better matches the measured coupling.

is aligned with one Tx and the output dc power is 100 W, the loss is 10 W with a 7 W contribution being from RF chokes. Hence for an output dc power of 100 W, 20 W is the total power lost in the inductors and 5 W in the other components, which confirms the advantages of using ZVS resonant converter based on Wide Band Gap semiconductors.

B. Coupled Inverters Characterization

Fig. 16 shows the measured dc-to-dc efficiency for a wide range of dc output powers. The lines are all well superimposed, validating experimentally the coupled inverter operation of providing the same dc output power and the same system efficiency regardless of the Rx position. From these plots it can be observed that the dc-to-dc system efficiency exceeds 60% as the output dc power is over 20 W.

A direct measurement of the Tx output currents $I_{o(n)}$ is not feasible since it strongly affects its operation, but it is possible to deduce that the currents through the active Tx coils are equal from Fig. 16 and from thermal measurements: if there was a change in the phases of the Tx coil currents due to a different Rx position, this would cause a significant increase of the inverter losses due to the degradation of the ZVS operation and would overheat Q_1. Indeed, a phase shift of the current $I_{o(n)}$ directly affects the inverter ability to operate in soft-

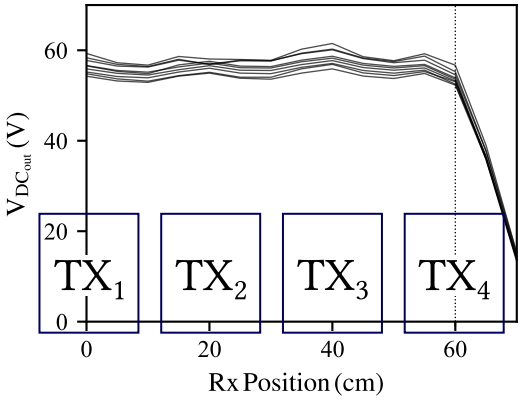


Fig. 14. $V_{DC_{out}}$ versus an extended Rx position, with the load as a parameter. Each line is a different dc load. For 0 cm, the Rx and TX_1 axes are aligned, and the couple TX_1 TX_2 is active; for 60 cm, the Rx and TX_4 axes are aligned and a further fifth coils should be activated (not available in the present prototype). Starting from this position the output voltage immediately drops.

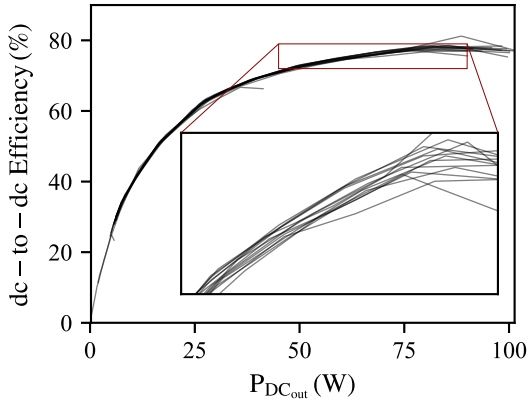


Fig. 16. Dc-dc efficiency as function of $P_{DC_{out}}$. For each position (a different line) the load is swept ($30 < R_L < 500$) to obtain the resulting output power range with a 70 V $V_{DC_{in}}$: this confirms that the position is not detuning the inverter.

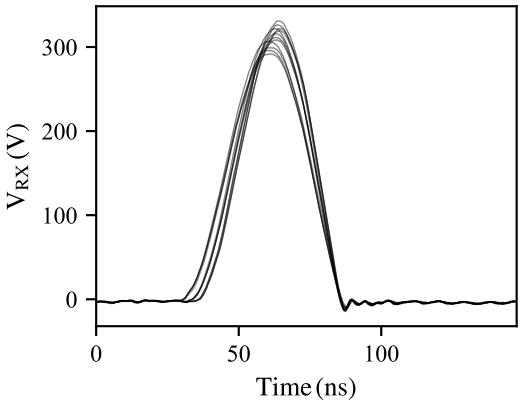


Fig. 15. Voltage on D_R (V_{RX}) measured for all the combination of four Rx positions (0, 5, 10, 15 cm) and three loads (60, 80, 120 Ω).

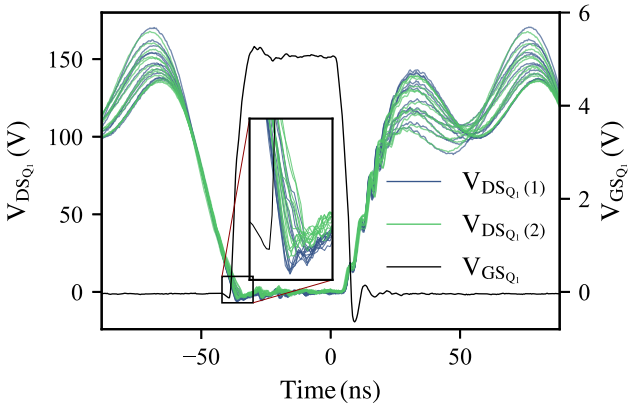


Fig. 17. GaN E-HEMT drain-source voltage of the inverters ($V_{DS_{Q1}(n)}$, with $n = 1, 2$) measured for four Rx positions (0, 5, 10, 15 cm) and three different loads (60, 80, 120 Ω). The measured gate-source driving voltage waveform ($V_{GS_{Q1}}$ is superimposed in the same plot: the load- and position-independent soft switching operation of the inverter is experimentally verified.

switching conditions, while the ZVS is guaranteed by the plots reported in Fig. 17, where the measured drain-source voltage waveforms of the two active inverters are reported, for various combinations of dc loads and Rx positions. The soft-switching operation is ensured for both inverters and therefore the desired phase coherence of the currents $I_{o(n)}$ is expected. Furthermore, tests carried out with the thermal camera confirm that no overheating is experienced by the GaN devices. A further confirmation comes from the measured constant $V_{DC_{out}}$ of Fig. 14, which proves the *virtual* series connection between the coupled inverters. Since the output voltage is related to the absolute value of V_{RX}:

$$V_{RX} = M_{TX_1} I_{o(1)} + M_{TX_2} I_{o(2)}, \tag{22}$$

a phase difference would add two out-of-phase contributions and therefore a lower V_{RX}, also dependent on the Rx position.

IV. Conclusions

The piece-wise modeling and design of a IPT system at 6.78 MHz for *on the move* powering has been presented. First the RF-to-RF link, consisting of an array of Tx coils and a moving Rx coil, is optimized. Each Tx coil is excited by a coupled load-independent Class EF Inverter, which ensures soft switching and constant output RF current, enforcing a *virtual* series connection. The receiving sub-system, based on a Class E rectifier, is designed embedded in the entire system to provide a quasi-resistive RF load to the inverter, while having constant output voltage.

The result is an optimized and fully modular dc-to-dc WPT system, capable of operating for several different Rx loading conditions and positions, which can be lengthened or shortened according to the specific application, without any need for further design efforts. With a dc input voltage of 70 V, the dc-to-dc efficiency is 80% and the dc output power is 100 W. Only the dc feed and the control logic are distributed along the path while the RF signal is generated locally, with the twofold benefit of minimizing the RF leakage and of providing full scalability.

REFERENCES

[1] W. Brown, "The History of Power Transmission by Radio Waves," *IEEE Transactions on Microwave Theory and Techniques*, vol. 32, no. 9, pp. 1230–1242, Sep. 1984.

[2] H. Kim, C. Song, D.-H. Kim, D. H. Jung, I.-M. Kim, Y.-I. Kim, J. Kim, S. Ahn, and J. Kim, "Coil Design and Measurements of Automotive Magnetic Resonant Wireless Charging System for High-Efficiency and Low Magnetic Field Leakage," *IEEE Transactions on Microwave Theory and Techniques*, pp. 1–18, 2016.

[3] M. Kazmierkowski and A. Moradewicz, "Unplugged But Connected: Review of Contactless Energy Transfer Systems," *IEEE Industrial Electronics Magazine*, vol. 6, no. 4, pp. 47–55, Dec. 2012.

[4] C.-S. Wang, O. Stielau, and G. Covic, "Design Considerations for a Contactless Electric Vehicle Battery Charger," *IEEE Transactions on Industrial Electronics*, vol. 52, no. 5, pp. 1308–1314, Oct. 2005.

[5] C.-S. Wang, G. Covic, and O. Stielau, "Power Transfer Capability and Bifurcation Phenomena of Loosely Coupled Inductive Power Transfer Systems," *IEEE Transactions on Industrial Electronics*, vol. 51, no. 1, pp. 148–157, Feb. 2004.

[6] T. Fujita, T. Yasuda, and H. Akagi, "A Dynamic Wireless Power Transfer System Applicable to a Stationary System," *IEEE Transactions on Industry Applications*, pp. 1–1, 2017.

[7] R. Trevisan and A. Costanzo, "A 1-kW Contactless Energy Transfer System Based on a Rotary Transformer for Sealing Rollers," *IEEE Transactions on Industrial Electronics*, vol. 61, no. 11, pp. 6337–6345, Nov. 2014.

[8] R. Trevisan and A. Costanzo, "A UHF Near-Field Link for Passive Sensing in Industrial Wireless Power Transfer Systems," *IEEE Transactions on Microwave Theory and Techniques*, vol. 64, no. 5, pp. 1634–1643, May 2016.

[9] F. Mastri, A. Costanzo, and M. Mongiardo, "Coupling-Independent Wireless Power Transfer," *IEEE Microwave and Wireless Components Letters*, vol. 26, no. 3, pp. 222–224, Mar. 2016.

[10] J. Shin, S. Shin, Y. Kim, S. Ahn, S. Lee, G. Jung, S.-J. Jeon, and D.-H. Cho, "Design and Implementation of Shaped Magnetic-Resonance-Based Wireless Power Transfer System for Roadway-Powered Moving Electric Vehicles," *IEEE Transactions on Industrial Electronics*, vol. 61, no. 3, pp. 1179–1192, Mar. 2014.

[11] T. Ohira, "The kQ Product as Viewed by an Analog Circuit Engineer," *IEEE Circuits and Systems Magazine*, vol. 17, no. 1, pp. 27–32, 2017.

[12] J. P. C. Smeets, T. T. Overboom, J. W. Jansen, and E. A. Lomonova, "Comparison of Position-Independent Contactless Energy Transfer Systems," *IEEE Transactions on Power Electronics*, vol. 28, no. 4, pp. 2059–2067, Apr. 2013.

[13] J. P. C. Smeets, T. T. Overboom, J. W. Jansen, and E. A. Lomonova, "Modeling Framework for Contactless Energy Transfer Systems for Linear Actuators," *IEEE Transactions on Industrial Electronics*, vol. 60, no. 1, pp. 391–399, Jan. 2013.

[14] F. Lu, H. Zhang, H. Hofmann, and C. C. Mi, "A Dynamic Charging System With Reduced Output Power Pulsation for Electric Vehicles," *IEEE Transactions on Industrial Electronics*, vol. 63, no. 10, pp. 6580–6590, Oct. 2016.

[15] A. Pacini, F. Mastri, R. Trevisan, D. Masotti, and A. Costanzo, "Geometry Optimization of Sliding Inductive Links for Position-Independent Wireless Power Transfer," in *2016 IEEE MTT-S International Microwave Symposium (IMS)*, May 2016.

[16] A. Pacini, F. Mastri, R. Trevisan, D. Masotti, and A. Costanzo, "Theoretical and Experimental Characterization of Moving Wireless Power Transfer Systems," in *2016 European Conference on Antennas and Propagation (EuCAP)*, Apr. 2016.

[17] Z. Zhang and K. T. Chau, "Homogeneous Wireless Power Transfer for Move-and-Charge," *IEEE Transactions on Power Electronics*, vol. 30, no. 11, pp. 6213–6220, Nov. 2015.

[18] M. Chabalko, J. Besnoff, M. Laifenfeld, and D. S. Ricketts, "Resonantly Coupled Wireless Power Transfer for Non-Stationary Loads With Application in Automotive Environments," *IEEE Transactions on Industrial Electronics*, vol. 64, no. 1, pp. 91–103, Jan. 2017.

[19] A. Pacini, S. Aldhaher, A. Costanzo, and P. D. Mitcheson, "Design of a Position-Independent End-to-End Inductive WPT Link for Industrial Dynamic Systems," in *2017 MTT-S International Microwave Symposium (IMS)*, Jun. 2017.

[20] *CST Microwave Studio 2013*, www.cst.com.

[21] S. Aldhaher, P. D. Mitcheson, and D. C. Yates, "Load-independent Class EF inverters for inductive wireless power transfer," in *2016 IEEE Wireless Power Transfer Conference (WPTC)*, no. 1, May 2016, pp. 1–4.

[22] M. K. Kazimierczuk and D. Czarkowski, *Resonant Power Converters*, 2nd ed. Hoboken, N.J: John Wiley & Sons, 2012.

[23] M. K. Kazimierczuk, "Analysis of Class E Zero-Voltage-Switching Rectifier," *IEEE Transactions on Circuits and Systems*, vol. 37, no. 6, pp. 747–755, 1990.

[24] J. Jozwik and M. Kazimierczuk, "Analysis and design of Class-E2 DC/DC converter," *IEEE Transactions on Industrial Electronics*, vol. 37, no. 2, pp. 173–183, apr 1990.

[25] J. A. Santiago-Gonzalez, K. M. Elbaggari, K. K. Afridi, and D. J. Perreault, "Design of Class E Resonant Rectifiers and Diode Evaluation for VHF Power Conversion," *IEEE Transactions on Power Electronics*, vol. 30, no. 9, pp. 4960–4972, Sep. 2015.



Alex Pacini received the Master Degree in Electrical and Telecommunication Engineering (summa cum laude) at the University of Bologna in 2015. He is currently a PhD student at the same university.

His research interests are in antenna systems, near-field wireless power transfer, resonant converters and RF/Microwave circuit and systems design.



Alessandra Costanzo is associate professor at the University of Bologna, Italy. She is currently involved in research activities dedicated to the wireless power transmission, adopting both far-field and near-field solutions, for several power levels and operating frequencies. She has authored more than 200 scientific publications on peer reviewed international journals and conferences and several chapter books. She is co-founder the EU COST action IC1301 WiPE "Wireless power transfer for sustainable electronics" where she chairs WG1: "far-field wireless power transfer". She is the chair of the MTT-26 committee on wireless energy transfer and conversion and member of the MTT-24 committee on RFID. She serves as associate editor of the IEEE Transaction on MTT, of the Cambridge International Journal of Microwave and Wireless Technologies and of the Cambridge International Journal of WPT. Since 2016 she is steering committee chair of the new IEEE Journal of RFID. She is MTT-S representative and Distinguished Lecturer of the CRFID, where she also serves as MTT-S representative. She is IEEE senior member.



Samer Aldhaher received the B.Sc. degree in electrical engineering from the University of Jordan, Amman, Jordan, and the Ph.D. degree from Cranfield University, Bedford, U.K., in 2010 and 2014, respectively.

His doctoral research focused on the design and optimisation of switched-mode circuits and development of novel electronic tuning methods for inductive power transfer applications. He is currently a Research Associate with the Control and Power Group, Department of Electrical and Electronic Engineering, Imperial College London. His current research interests include the design of multi-MHz DC/AC inverters and rectifiers and wireless power transfer applications based on resonant inductive links.



Paul D. Mitcheson (SM'12) received the M.Eng. degree in electrical and electronic engineering and the Ph.D. degree in micro-power motion based energy harvesting for wireless sensor networks from the Imperial College London, London, U.K., in 2001 and 2005, respectively. He is currently a Professor in Electrical Energy Conversion with the Control and Power Research Group, Electrical and Electronic Engineering Department, Imperial College London. His research interests include energy harvesting, power electronics, and wireless power transfer to provide power to applications in circumstances where batteries and cables are not suitable. His research has been supported by the European Commission, Engineering and Physical Sciences Research Council, and several companies. Prof. Mitcheson is a Fellow of the Higher Education Academy and is on the executive committee of the UK Power Electronics Centre.